INVITED REVIEW—International Conference on Nanoscience and Technology, China 2013

Functionalization of carbon nanotubes/graphene by polyoxometalates and their enhanced photo-electrical catalysis*

Zhang Shuang-Shuang(张双双)[a)b)], Liu Rong-Ji(刘荣基)[a)], Zhang Guang-Jin(张光晋)[a)†], and Gu Zhan-Jun(谷战军)[c)]

[a)] *Key Laboratory of Green Process and Engineering, Institute of Process Engineering, Chinese Academy of Sciences, Beijing* 100190, *China*
[b)] *University of Chinese Academy of Sciences, Beijing* 100049, *China*
[c)] *Key Laboratory for Biomedical Effects of Nanomaterials and Nanosafety, Institute of High Energy Physics, Chinese Academy of Sciences, Beijing* 100049, *China*

(Received 4 September 2013; revised manuscript received 14 March 2014; published online 10 June 2014)

Carbon nanotubes and graphene are carbon-based materials, which possess not only unique structure but also properties such as high surface area, extraordinary mechanical properties, high electronic conductivity, and chemical stability. Thus, they have been regarded as an important material, especially for exploring a variety of complex catalysts. Considerable efforts have been made to functionalize and fabricate carbon-based composites with metal nanoparticles. In this review, we summarize the recent progress of our research on the decoration of carbon nanotubes/graphene with metal nanoparticles by using polyoxometalates as key agents, and their enhanced photo-electrical catalytic activities in various catalytic reactions. The polyoxometalates play a key role in constructing the nanohybrids and contributing to their photo-electrical catalytic properties.

Keywords: carbon nanotube, graphene, polyoxometalate, photo-electro-catalysis

PACS: 88.30.rh, 78.67.Bf, 82.45.Jn **DOI:** 10.1088/1674-1056/23/8/088801

1. Introduction

Recently, the global energy crisis and environmental pollution have motivated researchers to develop various catalysts in renewable energy devices. Among these materials, carbon-based nanomaterials with graphene structures have received considerable attention due to their outstanding chemical and physical properties such as electrical conductivity, large specific surface area, thermal stability, and mechanical strength.[1–4] Carbon-based materials, especially one-dimensional (1D) carbon nanotubes (CNTs) and two-dimensional (2D) graphene (GN), are the most popular carbon-based materials, and have been widely used as catalysts or as the conducting supports of other catalysts.[5–8] It can be seen that the nanotechnology in decorating carbon nanotubes/graphene with multifunctional nanoparticles, especially metal nanoparticles (MNPs), has rapidly developed in the past few decades.

The metal nanoparticle has emerged as a new kind of compound that has attracted intensive attention due to its unique electronic, optical, magnetic, and catalytic properties.[9–11] To be specific, due to the fact that a nanoparticle has a high surface-to-volume ratio, the nanoparticles provide a great number of active sites per metal mass, and their flexible shapes and sizes enable them to provide ample corners, vertices, defects, kinks, and steps in the process of catalytic reactions.[12] However, pure MNPs are unstable and easily gather together,[9] which restricts their utility in the catalyst industry. These particles are therefore usually supported on a substrate to produce nanohybrids with a synergistic effect of the two functional materials.[13,14] During recent years, tremendous efforts have been made to develop the methods of assembling well defined, highly stable catalysts, including electroless plating,[15] electrodeposition,[16] and chemical deposition.[17]

Our group developed a more facile and easier strategy for the decoration of MNPs (Ag, Au, Pd, and Pt) on CNTs or GN with the help of polyoxometalates (POMs).[18–24] Polyoxometalates are early transition metal (mostly Mo, W, V, Nb) oxygen anionic clusters with discrete structure. They are good electron acceptors and can undergo reversible multielectron reduction reactions with intact structure remaining unchanged, thus they are widely used as novel green agents in homogeneous or heterogeneous catalytic processes.[25–28] Our earlier work has indicated that POMs show great potential applications in photo-electro-catalyst synthesis. Therefore, we present here a short review on our recent research in synthesis strategies, characterizations, and properties of these hybrids. The rest of this paper is organized as follows. The CNT-based and GN-based catalysts and their high photo-electrocatalytic activities toward different reactions are mainly discussed in Sections 2 and 3. Some conclusions are drawn in Section 4.

*Project supported by the National Natural Science Foundation of China (Grant No. 21371173) and the National Basic Research Program of China (973 Program) (Grant No. 2012CB932504).

†Corresponding author. E-mail: zhanggj@home.ipe.ac.cn

© 2014 Chinese Physical Society and IOP Publishing Ltd

2. Metal nanoparticle/POM/carbon nanotube tri-component hybrids

2.1. Synthesis and characterizations of MNP (Au, Pt, Ag)@POM–CNT nanohybrids

Metal nanoparticles, as an important member of the material family, have been applied in various fields, such as information storage, heavy metal ion sensors, biomedicine, and catalysis.[29–32] For the fabrication of MNPs, methods including thermal or photolytic decomposition,[33] photochemical reduction,[34] ionic liquid aided reaction,[35] and hydrogen plasma–metal reaction[36] have been developed. However, most of these reactions are complicated or have to be conducted in harsh conditions, which hampers the development of metal nanotechnology. Very recently, a simple process for the fabrication of MNPs using POMs has been introduced.[37–39] The whole process can be performed at room temperature and the process is atom economic, with all the reactant going to the final product. Inspired by this success, in 2010, we succeeded in the synthesis of Au NPs@POM–CNTs. In a typical experiment, $H_3PW_{12}O_{40}$ (PW12) without oxygen was first mixed with isopropanol. Then the solution was irradiated under UV light. After this, the as-prepared solution of MWCNTs and MNPs ($HAuCl_4$, H_2PtCl_4, $AgNO_3$) salt solution was added to the reduced PW12 at room temperature with soft shaking by hand. Several minutes later, the tri-component nanohybrid was prepared.[18–20]

Figure 1 illustrates scheme 1 for the synthesis procedure of the Au NPs@POM–CNTs. The product was separated from the solvent by centrifugation and washed with deionized water. The morphology of the nanohybrid was investigated by transmission electron microscopy (TEM). Figure 2 shows the images of the bare CNTs (Fig. 2(a)) and well defined Au NPs@POM–CNTs (Fig. 2(b)). The magnified image reveals that the average size of the Au NPs is about 35 ± 3 nm (Fig. 2(c)) with a clear core–shell nanostructure (Fig. 2(d)). This interesting structure has been reported elsewhere.[37,39–41] High resolution TEM (HRTEM) shows its highly mono-crystalline characteristic; the lattice fringe of the Au(111) crystalline face (0.23) is observed in Fig. 2(e). To further corroborate the existence of the POM, *in situ* energy dispersive X-ray spectroscopy (EDX) was employed (Fig. 2(f)). As we can see, besides strong peaks of Au, tungsten peaks can also be seen, confirming the POM around Au NPs. The actual Au loading of the hybrid was determined to be about 29.1 wt% by inductively coupled plasma–mass spectroscopy (ICP-MS).

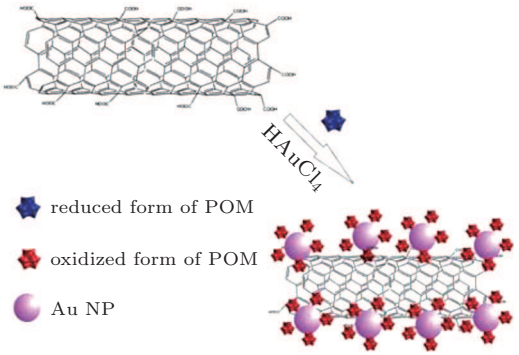


Fig. 1. (color online) Scheme 1 for the Au NP@POM–CNT synthesis route at room temperature. Reproduced with permission from Ref. [18].

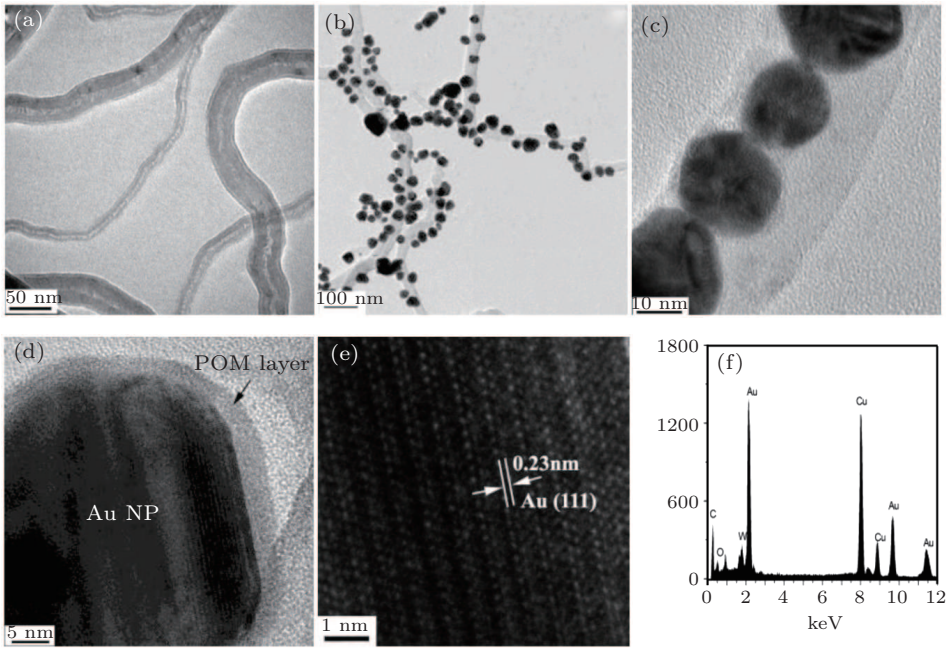


Fig. 2. (a) TEM image of bare CNTs; (b) Au NP@POM–CNT composites; (c) four aligned Au NPSs on the surface of a single CNT; (d) magnified image of one Au NP@POM core–shell structure; (e) HRTEM image of a single Au NP. Reproduced with permission from Ref. [18].

As an extension of this work, we successfully modified the CNTs with well defined Pt (2.5 ± 0.5 nm) and Ag (5.0 ± 0.5 nm) NPs. EDX and X-ray photoelectron spectroscopy (XPS) were both used to determine the formation of the tri-component hybrid of Pt NPs@POM–CNTs and Ag NPs@POM–CNTs. The actual Pt and Ag loadings of the hybrids were determined to be about 18.1 wt% and 33.1 wt% respectively, which are close to the initial design loadings (20 wt% and 36 wt%).

2.2. Enhanced photo-electrical catalysis

The CNT-based materials take advantage of each component to obtain new materials with enhanced properties with a view toward many challenging reactions.

2.2.1. High photocatalytic activity of Au NPs@POM–CNTs under visible light

POMs are regarded as green photocatalysts under the irradiation of UV light. Visible light hardly promotes the reaction, especially for PW12 in general conditions. It was surprising for us to find that the as-prepared Au NP@POM–CNT nanohybrids showed significant photo-catalytic activities under visible light irradiation ($\lambda > 420$ nm).

Figure 3 shows the comparison among the curves of the decrease in rhodamine B (RhB) concentration versus time in different catalytic circumstances. None of the pure components show their photocatalytic activity. When combining the Au NPs and POM, a notable photocatalytic activity can be observed under visible light, though the efficient is relatively low.

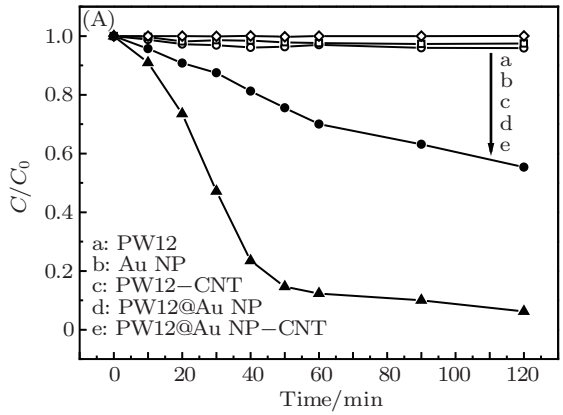


Fig. 3. Temporal evolutions of the photodegradation of RhB of different catalytic materials under visible light irradiation ($\lambda > 420$ nm). Reproduced with permission from Ref. [18].

To elaborate the mechanism of our system, we start with the photocatalysis process of the semiconductor. When the semiconductor is irradiated by energy higher than or equal to its band gap (E_g), holes (h^+) in the valence band and electrons (e^-) in the conduction band are formed. The positive holes (h^+) can directly react with a substrate to oxidize it or to form strongly oxidizing hydroxyl radicals (·OH) in the presence of water. Hydroxyl radicals and/or h^+ are regarded as the oxidizing species, and they are the primary actors for the degradation of the organic substrates. Electrons are trapped by oxygen molecules that can subsequently react with water to form hydroxyl radicals also (Fig. 3). Moreover, the electrons can also directly reduce the substrate (Scheme 2, Fig. 4).[42]

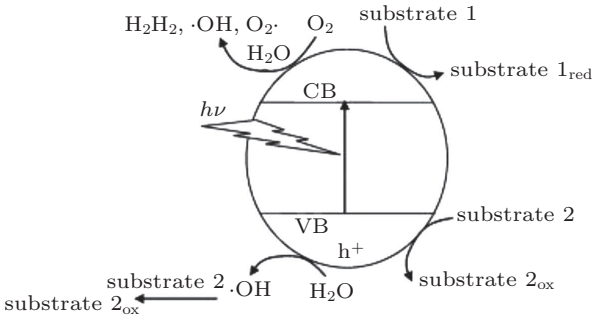


Fig. 4. Scheme 2 for mechanism of the photocatalytic reaction by using a semiconductor as a photocatalyst. Reproduced with permission from Ref. [42].

By analogy, when referring to the Au NP@POM–CNT system, the following explanation may be reasonable to explain its high photocatalysis (Scheme 3). The electronic characteristics of POM and semiconductor are analogous, thus POM exhibits semiconductor-like photochemical behaviors.[26] When irradiated by the UV light, the electron transfers from the O^{2-} ion to a W^{6+} ion in W–O–W bands, resulting in formation of a pair of a hole (O^-) and a trapped electron (W^{5+}). The W^{5+} can further be oxidized by oxygen, the O^- can serve as an oxidant for a solution species, and this forms a photocatalytic cycle. When Au NPs are assembled on POMs, the surface plasmon resonance (SPR) of Au NPs is excited, inducing charge transfer from Au NPs to POM. The Au^+ further catalyzes oxidation of organic pollutants. However in the Au NP@POM system, charge recombination occurs easily due to the close affinity between the Au NPs and POM, which can reduce the efficiency of photocatalysis. The introduction of CNTs enhances the separation between photo-induced holes and electrons. The electrons trapped on CNTs can further be oxidized by the oxygen, forming another new cycle.

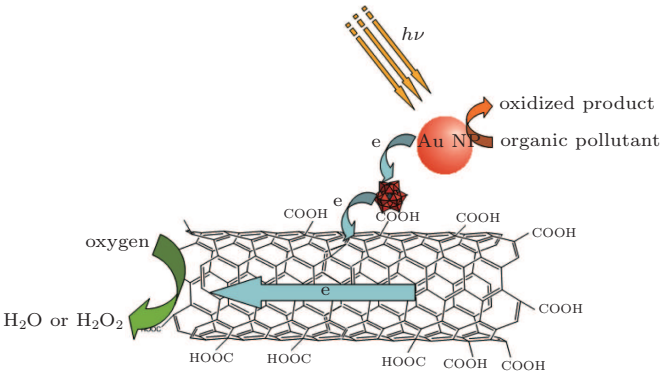


Fig. 5. (color online) Scheme 3 for the photocatalytic mechanism of Au NP@POM–CNT tri-component nanohybrid. Reproduced with permission from Ref. [18].

When we replace the CNTs with CdS quantum dots (QDs), the tri-component CdS QDs–Au NPs@POMs are obtained. This composite shows high photocatalytic activity in the photoproduction of H_2 and in the degradation of RhB and methyl orange under visible irradiation.[43] This nanohybrid is analogous to the Au NPs@POM–CNTs, but the role played by CdS is different from that played by the CNTs. In this system, photoexcitation of the CdS QDs causes the electron to transfer from the valence band (VB) to the conduction band (CB), yielding electron–hole pairs. As CdS QDs are assembled with POM, the electrons transfer from the CB of CdS QDs to the lowest unoccupied molecular orbital (LUMO) of the POMs, and then further transfer to the Au NPs. Such an electron transfer enhances the separation between photo-induced holes and electrons, and thus the photocatalytic activities are improved significantly (Scheme 4, Fig. 6).

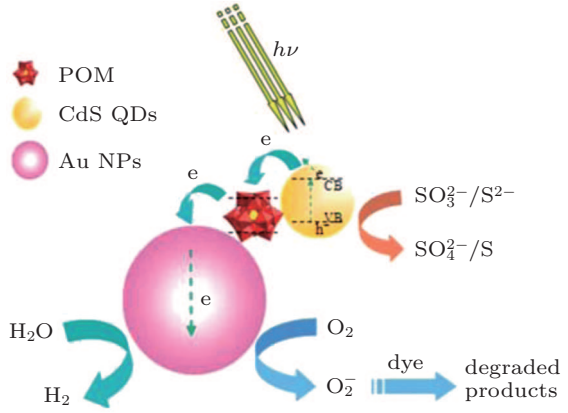


Fig. 6. (color online) Scheme 4 for the photocatalytic mechanism of the CdS QD–Au NP@POM nanohybrid. Reproduced with permission from Ref. [26].

2.2.2. Ag NP@POM–CNT hybrids as high-performance electrocatalyst for oxygen reduction reaction in alkaline medium

For most fuel cells, the oxygen-reduction reaction (ORR) is considered one of the most difficult and important reactions. The sluggish kinetics of the ORR accounts for a significant part of the high cost.[44] Pt or Pt alloy is the most widely used electrocatalyst for the ORR; however, its high cost and instability due to long-time immersion in alkaline medium restrict its application. Much research work has been done to discover cheaper metals to replace the Pt. It is reported that silver has a high catalytic activity toward the oxygen reduction reaction and perhydroxyl ion decomposition in alkaline conditions. For this reason, silver has been considered to be a potential metal to replace Pt.[45–47] Inspired by this, our team has synthesized the Ag NPs@POM–CNTs, which show catalytic activity toward the ORR.

The ORR in alkaline solution can proceed in two ways.

(i) Direct four-electron pathway. O_2 is reduced to OH^- ions through the following reaction:

$$O_2 + 2H_2O + 4e^- \rightarrow 4OH^-. \quad (1)$$

(ii) Two-electron pathway. O_2 is reduced to HO_2^- ions through the reaction

$$O_2 + H_2O + 2e^- \rightarrow HO_2^- + OH^-, \quad (2)$$

followed by another two-electron reduction of peroxide ions to OH^- ions through the reaction

$$HO_2^- + H_2O + 2e^- \rightarrow 3OH^-, \quad (3)$$

or the decomposition reaction:

$$2HO_2^- \rightarrow 2OH^- + O_2. \quad (4)$$

A key criterion to determine a good catalyst is that the reaction occurs through the direct four-electron pathway.

The electrochemical experiments show that the materials exhibit catalytic activities toward ORR in the O_2-saturated solution. Compared with the bare CNTs and pure Ag NPs, the Ag NPs@POM–CNTs have cathode peaks that show a significant positive shift and a higher current density. As the current density and onset potential are the most two important parameters to evaluate the activity of the electrocatalysts, our data prove that the higher the Ag loading, the better the catalytic activity is. What is more, only one current peak is observed for nanohybrid modified electrodes, while two oxygen reduction peaks can be observed for the pure CNTs and Ag modified electrodes. These voltammetric characterizations reveal that a four-electron reaction occurs for oxygen reduction on Ag NP@POM–CNT nanohybrids, but the less efficient two-step reactions occur on the pure CNTs and Ag modified electrodes. The methanol interruption test prove that our material is hardly influenced by the methanol, which means that, even if working in a methanol-tolerant solution, our prepared nanohybrids still exhibit their high electrocatalytic activity.

The number of exchanged electrons for the ORR is evaluated from the Koutecky–Levich plots (j^{-1} versus $\omega^{0.5}$) drawn from the linear sweep voltammetry (LSV) patterns and determined by the following equation.[48,49]

$$\frac{1}{j} = \frac{1}{j_k} + \frac{1}{B\omega^{0.5}}, \quad (5)$$

where j is the measured current density at a given potential, j_k is the kinetic current density, and ω is the electrode rotation rate. Therefore, $1/B$ is the calculated slope and it is in mA^{-1} cm^2 $rpm^{0.5}$. B could be determined from the slope of Koutecky–Levich plots based on the Levich equation:

$$B = 0.2nF(D_{O_2})^{2/3}\upsilon^{-1/6}C_{O_2}, \quad (6)$$

where n is the number of electrons transferred per oxygen molecule, F is the Faraday constant (expressed as $F = 96485\ C \cdot mol^{-1}$), D_{O_2} is the diffusion coefficient of O_2 in

0.1-M NaOH (1.99×10^{-5} cm$^2 \cdot$ s^{-1}), υ is the kinetic viscosity (0.01 cm$^2 \cdot$ s^{-1}), C_{O_2} is the bulk concentration of O_2 (1.2×10^{-6} mol $\cdot$ cm^{-3}), and the constant 0.2 is adopted when the rotation speed is expressed in rpm.[50]

Figure 7 shows representative LSV curves on the RDE electrode of all the nanohybrids and Pt–CNTs. We can see that, although the onset potential of ORR of the 36% Ag NPs@POM–CNTs is still lower than that of the 36% Pt–CNTs, the limiting diffusion current density of the hybrid is slightly higher than that of 36% Pt–CNTs. The stabilities of Ag NP@POM–CNT and Pt–CNT electrodes are examined by chronoamperometry experiments monitored with the potential set at −0.4 V versus SCE for 1.3×10^4 s (Fig. 8). After the experiment, 80.6% of the initial current was left for the Ag NP@POM–CNT electrocatalyst, while the corresponding value for the Pt–C electrocatalyst is 60.1% of the initial current. Thus, our results sufficiently prove that the as-prepared nanohybrids are competitive with the Pt–CNTs.

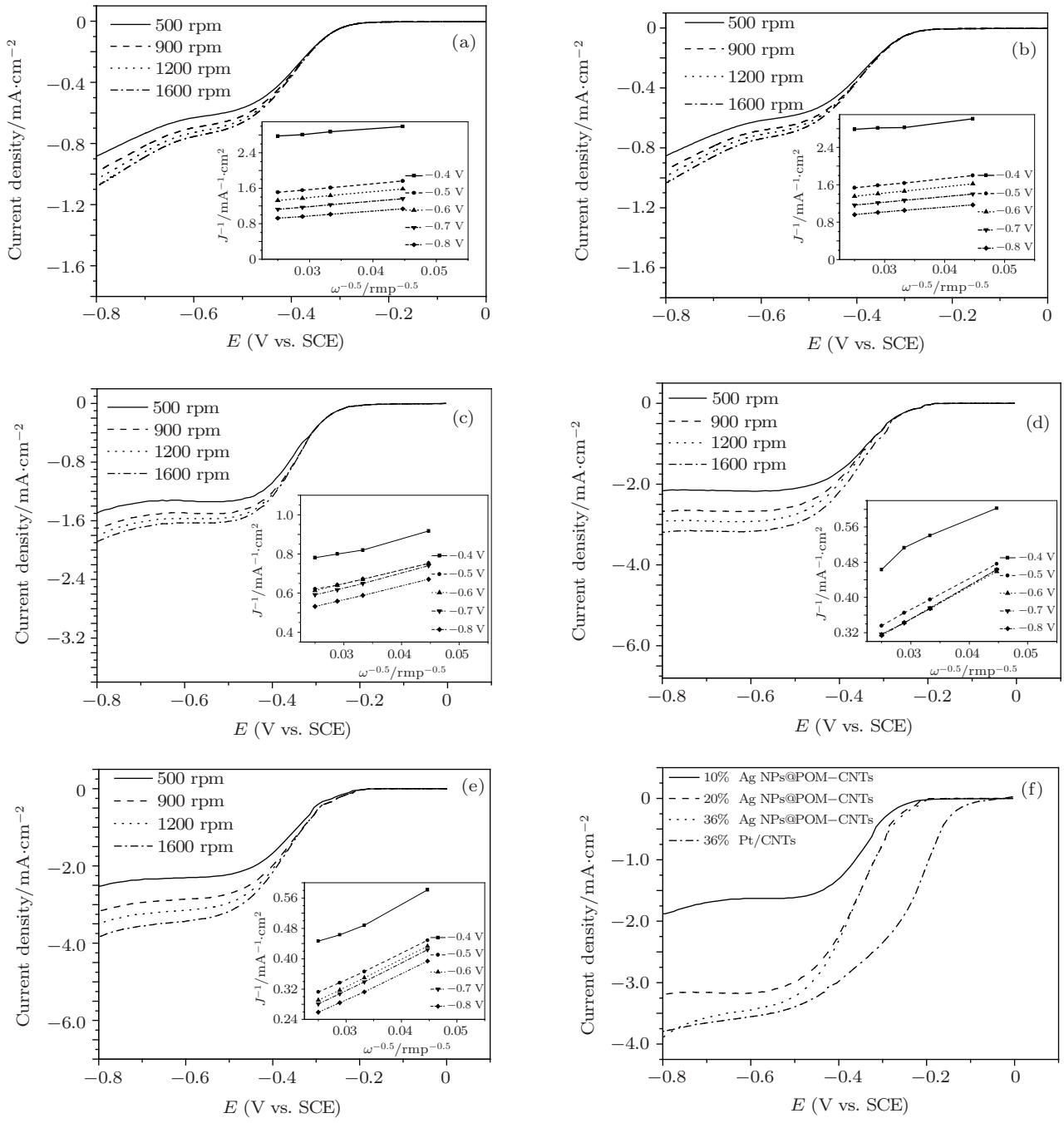


Fig. 7. LSV curves of ORR at various rotation rates for bare CNTs (a), Ag NPs (b), 10% Ag NPs@POM–CNTs (c), 20% Ag NPs@POM–CNTs (d), and 36% Ag NPs@POM–CNTs (e) in O_2 saturated 0.1-M NaOH solutions at a scan rate of 10 mV s^{-1}. Insets show the Koutecky–Levich plots for the five electrode materials at various potentials. (e), (f) LSV curves of ORR in O_2 saturated 0.1-M NaOH solutions at a scan rate of 10 mV s^{-1}. The rotation rate is 1600 rpm. SCE is the abbreviation for saturated calomel electrode. Reproduced with permission from Ref. [20].

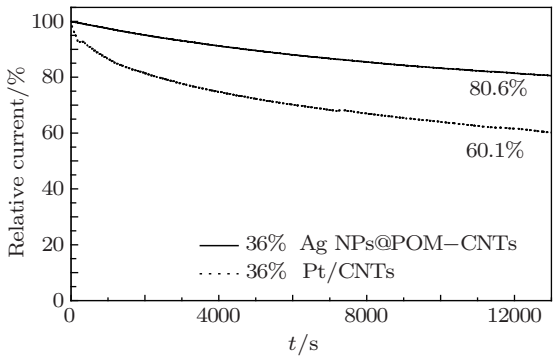


Fig. 8. Current–time (i–t) chronoamperometric response of 36% Ag NP@POM–CNT and 36% Pt–CNT modified GC electrodes at −0.4 V versus SCE in O_2 saturated 0.1-M NaOH at a rotation rate of 1600 rpm. Reproduced with permission from Ref. [20].

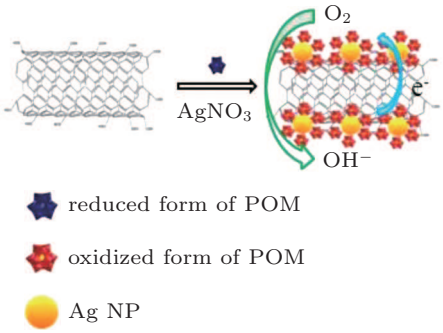


Fig. 9. (color online) Scheme 5 for the electrocatalytic mechanism of Ag NP@POM–CNT tri-component nanohybrid. Reproduced with permission from Ref. [18].

According to the previously reported results,[51–54] the building up of positive charge on CNT surfaces provide sites for the side-on O_2 surface adsorption. The diatomic adsorption can weaken the O–O bonding and facilitate the direct reduction of oxygen into OH^- via a four-electron process. In our systems, POMs serve as bridging molecules between Ag NPs and CNTs. In addition, POMs are also an important co-catalyst that facilitates the charge transfer from the nanotube to the Ag NPs, resulting in a high positive charge quantity on the CNTs, and this may facilitate the ORR activity enhancement. Moreover, Ag with enough electrons on its surface as the main reaction sites easily adsorbs O_2 and promotes the ORR (Scheme 5, Fig. 9).

2.2.3. The high electrocatalytic performance of Pt NPs@POM–CNTs for electrode reaction

The low operating temperature and rapid response to change in load make the methanol fuel cell one of the most promising technologies for energy generation.[55] In fact, there are some drawbacks, such as the low kinetics of methanol electro-oxidation on the anode.[56] The challenge is to elaborate efficient catalysts for the anode. For this purpose, we used the Pt NP@POM–CNT tri-component hybrid as the methanol oxidation catalyst. To investigate the electrocatalytic activity toward methanol oxidation, the catalytic properties of Pt–carbon black with the same Pt loading (20 wt%) and various reported Pt NP–CNT systems that were prepared with different methods were also examined for comparison. Table 1 shows some principal parameters for methanol oxidation evaluation. From the table, we can see that the values of both the mass activity and I_f/I_b of the Pt NPs@POM–CNTs are higher than those of other Pt-based nanomaterials, indicating that Pt NPs@POM–CNTs exhibit higher electrocatalytic activity for methanol oxidation.[57] In addition, the onset and peak potential of the methanol oxidation of Pt NPs@POM–CNTs show a negative shift, which further proves the enhanced activity of the nanohybrid. Moreover, the prepared nanohybrid also shows better stability according to our long-term circle experiment data. All the above data reveal that Pt NPs@POM–CNTs possess excellent electrocatalytic activity and resistance toward methanol poisoning. We attribute the better performance of the nanohybrid of Pt NPs@POM–CNTs to the following three major factors: (i) the high conductivity of CNTs accelerates the electron transfer between target molecule and electrode, (ii) well defined Pt NPs with small size are beneficial to their electrocatalytic activity, (iii) the existence of a layer of POM around Pt NPs may be helpful for the electrocatalytic activities and anti-poisoning properties of the catalyst.

Table 1. Voltammetric characteristics of CH_3OH oxidation in 0.5-M H_2SO_4 on glassy carbon electrodes variously modified with Pt nanoparticles (NPs). The scan rate is 50 $mV \cdot s^{-1}$.

Electrode	E^a_{onset}/V	E^a_f/V	I_f/(mA/mg Pt)	I_f/I_b	References
Pt@POM–CNTs	0.24	0.62	431	1.86	[19]
Pt–carbon black	0.31	0.66	137	0.97	[19]
Pt–CNTs	0.20	0.64	96	1.42	[58]
Pt–IS-ILs[b]–CNTs	∼ 0.38	∼ 0.65	∼ 410	∼ 0.95	[59]
Pt–PDDA[c]–CNTs	∼ 0.32	∼ 0.70	∼ 241	∼ 1.0	[59]
Pt–DMF–dipyridine–CNTs	∼ 0.29	∼ 0.66	∼ 160	∼ 1.2	[60]

[a]potentials versus saturated calomel electrode (SCE).

[b]IS-ILs: imidazolium-salt-based ionic liquids.

[c]PDDA: polydiallyldimethylammonium.

2.3. Brief summary

Our work opens a new way to decorate CNTs with NPs. The catalysts combine the advantageous electrical and mechanical properties of CNTs with the electronic, optical, magnetic, and catalytic properties of the metal NPs, achieving an enhanced photo-electrocatalysis toward various reactions. They are potential materials for solar energy application, fuel cells, and waste water treatment. Various carbon-based supports can be used to create new materials on the basis of our work.

3. Metal nanoparticle–polyoxometalates–graphene tri-component hybrids

Graphene (GN) is a 2D single-atom-thick carbon crystal with a honeycomb lattice structure. It has gained broad and interdisciplinary attention since it was discovered. Compared with other carbon allotropes, graphene possesses several genuine advantages, such as higher theoretical specific surface area (2630 $m^2 \cdot g^{-1}$), superior electron mobility (2×10^5 $cm^2 \cdot V^{-1} \cdot s^{-1}$), and locally conjugated structure.[61–63] These provide graphene with a dominant position to replace carbon nanotubes as a more efficient catalyst or supporting material for catalysts.

With the same synthesis route as indicated in Section 2, we use graphene replaced carbon nanotubes to synthesize a series of *M*NPs@POM–GN (*M* = Au, Pt, Pd) and Ag nanonet@POM–GN with an interesting surface topography looking like tiny threads. All the experiments have proven that the synergic effect induces a remarkable enhancement of the catalytic properties. In this section we will focus our attention mainly on the characterization and unusual catalytic activity of the as-prepared graphene-based materials in some challenging reactions. Anyone who is interested in the synthesis strategy should refer to Section 2 or Refs. [21], [22], and [24].

3.1. Characterization

Figure 10 shows Scheme 6, that features the one-step preparation procedure of the Au NP@POM–GN nanohybrids. Figure 11 shows typical TEM images of Au NPs@POM–GN. As expected, Au NPs (15 ± 3 nm) are uniformly dispersed on the crumpled GN (Figs. 11(a) and 11(b)). The magnified image reveals that the Au nanoparticles are surrounded by a thin layer of PW12, showing an Au NP@POM core–shell structure (Fig. 11(c)). The HRTEM image of a single Au NP displays its highly mono-crystalline characteristic; the lattice fringe of the Au (111) crystalline face (0.23 nm) can also be seen in this figure. The EDX data demonstrate the presence of POM and Au NPs. The Au loading of the hybrids is determined to be ca. 35 wt%.

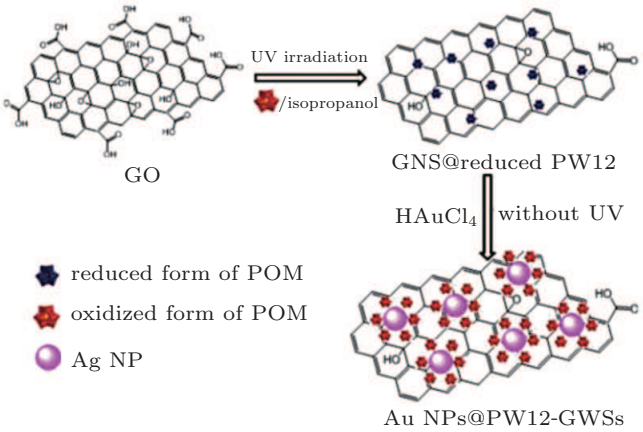


Fig. 10. (color online) Scheme 6 for the preparation procedure of the representative tri-component Au NP@POM–GN hybrids. Reproduced with permission from Ref. [21].

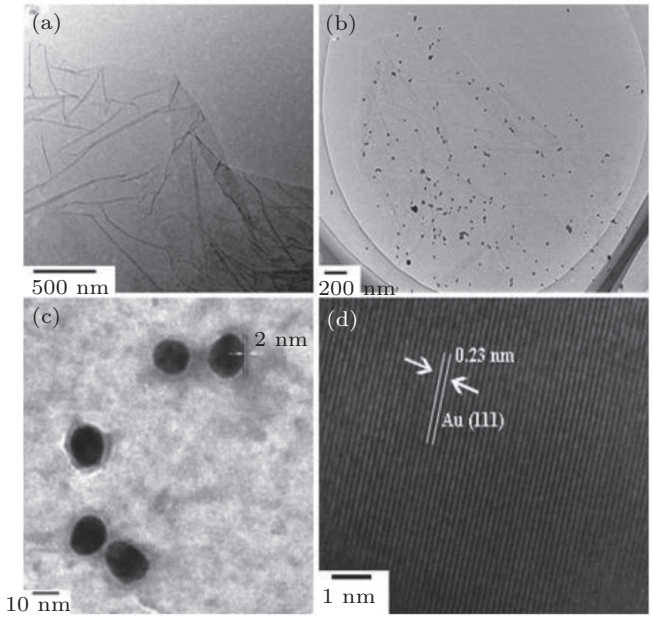


Fig. 11. TEM images of (a) bare G nanosheets; (b) 39.6% Au NP@POM–GN composites; (c) magnified GN image of five Au@POM core–shell structures; (d) HRTEM image of single Au NP. Reproduced with permission from Ref. [21].

The same detection methods have been employed to characterize Pd NPs@POM–GN and Pt NPs@POM–GN. The GN is successfully decorated with the Pd (4 nm–8 nm) or Pt (4 nm–5 nm) NPs. Loadings of the Pd and Pt are about 21.7 wt% and 20.2 wt% respectively. XPS combined with XRD is used to monitor the degree of GO photoreduction and the change of the chemical composition of the Au NPs@POM–GN, PdNPs@POM–GN, and Pt NPs@POM–GN.[21,24] From XPS we can see that all the peaks corresponding to the oxygen containing groups decrease after photoreduction, indicating that most of the groups are removed. Due to the restoration of the sp^2 carbon network, the graphitic-like C content is increased. The content values of the different types of carbon and corresponding value changes of GO and nanohybrids are calculated in Table 2.

Table 2. Fitting of the C 1s peak binding energy (eV) (relative atomic percentage %).

GO	284.8 (38.6%)	286.8 (60.2%)	287.8 (0.77%)	288.8 (0.43%)
PtNPs@POM–GN	284.8 (69.1)	286.8 (30.6%)	287.8 (0)	288.6 (0.3%)
PdNP@POM–GN	284.8 (80.2%)	286.8 (19.8%)	287.8 (0)	289 (0)

The Raman spectrum provides the information about the defects and structural properties of the materials. For GO and the three hybrids, two fundamental vibrations, G band and D band, are observed. The G and D bands refer to the scattering of the E_{2g} mode of sp^2 carbon atoms and the intervalley scattering of sp^2 carbon atoms respectively. The intensity ratio of D to G bands (I_D/I_G) is a measure of the disorder degree and average size of the sp^2 domains. When G is oxidized to GO, the intensity ratio changes from 0.129 to 0.949, proving the presence of defects and the diminution in size of the sp^2 domains. The values of the ratio I_D/I_G of Au, Pd, and Pt NPs@POM–GN are 0.813, 0.853, and 0.694 respectively, which is far below that of the GO (0.956). As this ratio is proportional to the average size of the sp^2 domains, these observations indicate that the photoreduction increases the average size of the crystalline graphene domains, which is attributed to the graphitic 'self-healing' in the hybrids.

In our earlier work, we synthesized 0D Ag NPs @POM–CNTs, showing catalytic activity for the oxygen reduction reaction. As is well known, the electrocatalytic activity strongly depends on the structure of the catalyst. It is proven that 1D Ag nanowires show higher electrocatalytic activity than 0D nanoparticles.[64,65] However, the low aspect ratio restricts their performance. Thus, a 2D Ag nanosheet is adopted because of its better electrical and thermal conductivities, as well as electrocatalytic stability.[66] Using the same method, we discover that POM is conducible to the preparation of 2D Ag nanosheet@POM–GN hybrids.[21] The POM reduces the Ag^+ and GO, and coats the resulting NN and GN at the same time.

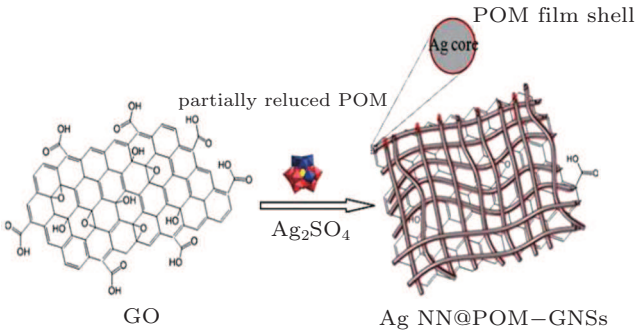


Fig. 12. (color online) Scheme 7 for the preparation procedure of the representative tri-component 2D Ag NN@POM–GN hybrids. Reproduced with permission from Ref. [22].

Figure 12 shows Scheme 7 for the preparation procedure for Ag NN@POM–GN nanohybrids. Figure 13 shows the typical SEM and TEM images of the prepared ternary Ag NN@POM–GN nanohybrid. From Figs. 13(a) and 13(b) we can see that the Ag NWs (40 nm–50 nm in diameter), with lengths exceeding 100 μm, disperse on the spreading graphene sheets, assembling the Ag nanosheets. The core–shell structure can be clearly observed in Fig. 13(c), which is in accordance with our other studies.[18–20] The HRTEM image and the electronic diffraction of the nanowires manifest their high crystallinity (Fig. 13(d)).

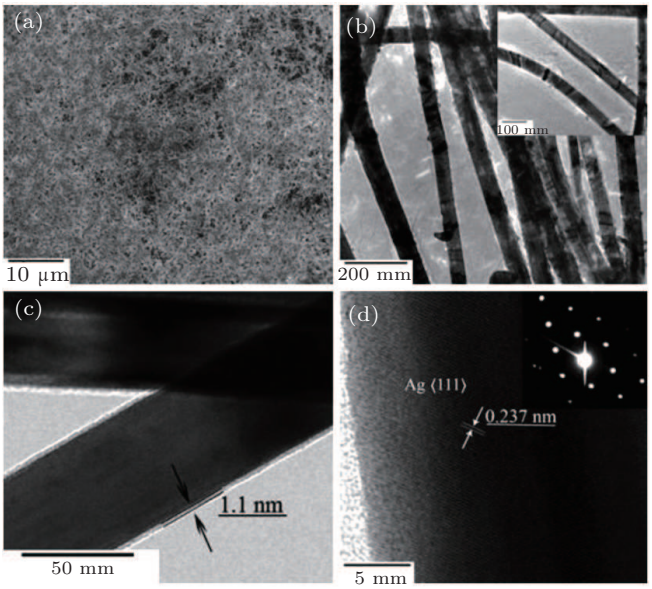


Fig. 13. (a) Typical SEM image of as-obtained Ag NN@POM–GN. (b) TEM image of Ag NN@POM–GN; the inset shows a magnified picture. (c) Magnified TEM image of core–shell Ag NW@POM structures. (d) HRTEM of one Ag NW; the inset shows the electronic diffraction of the nanowires. Reproduced with permission from Ref. [22].

3.2. Enhanced catalytic activities for challenging reactions

3.2.1. Enzyme-free electrochemical biosensor for hydrogen peroxide

H_2O_2 is a by-product of many oxidative biological reactions, including those of glucose oxidase, cholesterol oxidase, uricase, alcohol oxidase, galactose oxidase, sarcosine oxidase, and L-amino-acid oxidase.[67–69] Therefore, an elaborate efficient enzyme-free sensor for H_2O_2 with high sensitivity, long stability, large detection range, and good selectivity is important for many fields. In this respect, we have synthesized Au NP@POM–GN tri-component hybrids as enzyme-free electrocatalysts for H_2O_2 detection.[21] Experiments including CV and amperometry in an argon-saturated pH 7 phosphate buffer are conducted to assess the electrocatalytic activity of the hybrids towards H_2O_2 electroreduction (Fig. 14). The three CV patterns clearly show that the catalytic reduction reaction of H_2O_2 by Au NPs@POM–GN occurs at a more positive (ca. +0.150 V) voltage and with a higher current, which is equivalent to saying that the hybrid has a higher catalytic activity toward H_2O_2 reduction.

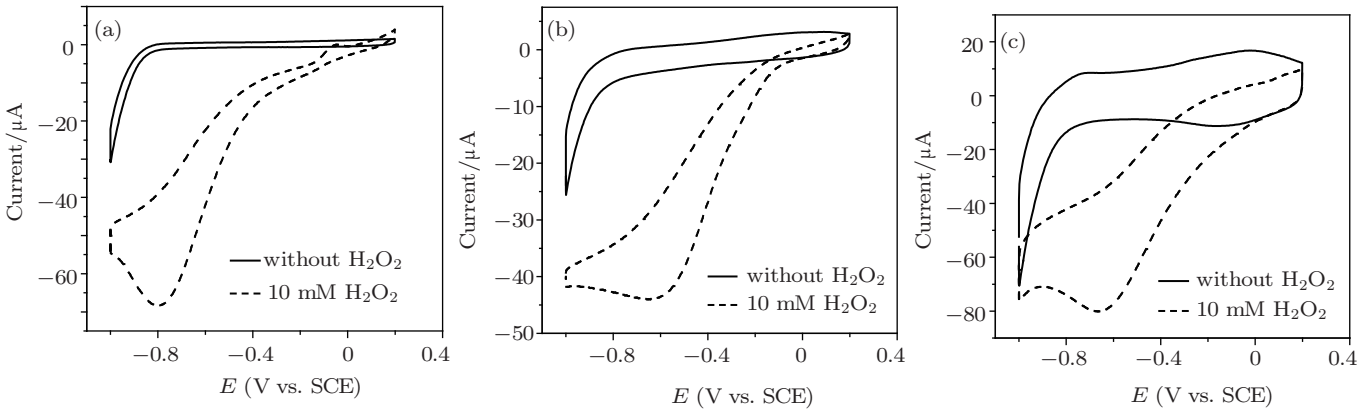


Fig. 14. CV curves of Au NPs@POM (a), 24.7% Au NPs@POM–GN (b), and 39.6% Au NPs@POM–GN (c) in Ar-saturated 0.4-M PBS (pH = 7) solutions without (solid line) and with (dotted line) 10-mM H_2O_2 at a scan rate of 50 mV·s^{-1}. Reproduced with permission from Ref. [21].

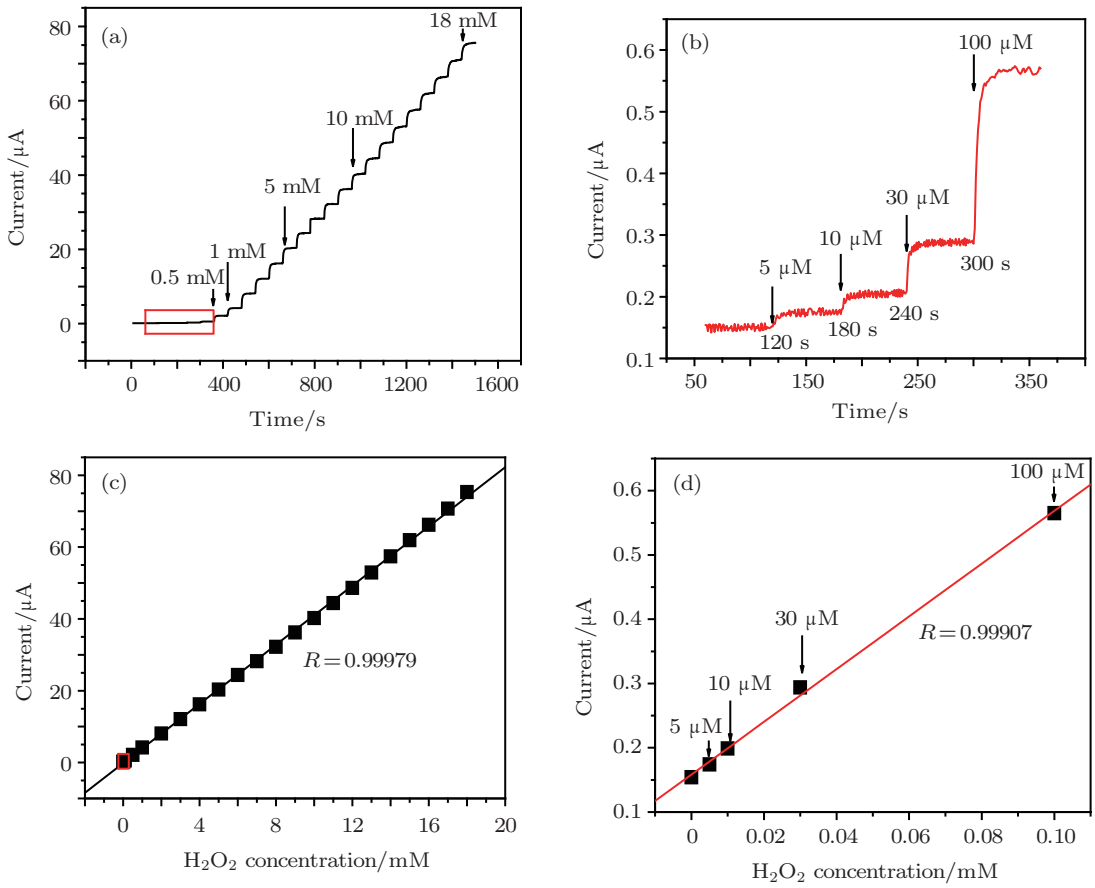


Fig. 15. (color online) Typical amperometric responses of the 39.6% Au NP@POM–GN modified electrode to successive addition of aliquots of H_2O_2 at −0.65 V versus SCE in 0.4 M PBS solution (pH 7.0) (a) and the corresponding calibration plot of steady-state currents against concentrations of H_2O_2 (c); (b), (d) local images corresponding to the rectangular areas of (a) and (c), respectively. Reproduced with permission from Ref. [21].

Figure 15(a) shows information about the current–time plot of the 39.6% Au NP@POM–GN modified electrode to successive addition of aliquots of H_2O_2. The steady-state current responses appear within ca. 3 s (at −0.650 V versus SCE) when the H_2O_2 is added, and with the successive additions the reduction current increases correspondingly. Moreover, when the H_2O_2 concentration is as low as 5 μM, obvious current responses could still be observed (Fig. 15(b)). Figure 15(c) shows the calibration curve, indicating a linear response range (LRR) from 5×10^{-6} M to 1.8 $\times10^{-2}$ M with a linear regression equation (LRE) of I (I_A) = $4.12C$(mM) − 0.18 (R = 0.99979), a limit of detection (LOD) of 1.54 μM (based on

S/N = 3) and a sensitivity of 58.87 $\mu A \cdot cm^{-2} \cdot mM^{-1}$. Figure 15(d) is a local magnified image corresponding to the rectangular area of Fig. 15(c). It is found that when the amount of Au increases the sensitivity of the catalyst increases correspondingly. We also compare the Au NPs@POM–GN with other Au-based biosensors. The result suggests that our hybrid is an extremely good biosensor for H_2O_2 detection, with a wider LRR, a relatively low LOD, and fast current response. The selectivity and stability experiments also confirm that the Au NPs@POM–GN has a wonderful selectivity and stability. It is worth mentioning that, although the present POM undergoes transformation in a pH 7 medium[57] and in the presence of H_2O_2,[58] our experimental results indicate that the transformation of the POM does not affect the electrocatalytic activity of the hybrids.

According to the literature, the mechanism for H_2O_2 electro-reduction is as follows:

$$H_2O_2 + e^- \rightarrow OH_{ad} + OH^-, \quad (7)$$

$$OH_{ad} + e^- \rightarrow OH^-, \quad (8)$$

$$2OH^- + 2H^+ \rightarrow 2H_2O. \quad (9)$$

GN and Au NPs are both good electron transporters within their structures, and the combination of Au NPs and GN further enhances their electron transport capacity. As a consequence, it can be hypothesized that the superior catalytic activity of the nanohybrids toward H_2O_2 may be mostly attributed to a synergistic effect of GN and Au NPs.

3.2.2. 2D Ag NN@POM–GN hybrids as high-performance electrocatalyst for oxygen reduction reaction in alkaline medium

As is well known, the electrocatalytic efficiencies of most reactions depend strongly on the structure, shape, and size, as well as the specific surface and crystallinity of the electrocatalyst. In our earlier work we have synthesized tri-component Ag NPs@POM–CNTs, showing catalytic activity for ORR. As an extension of the work, we also synthesize hybrid Ag NNs@POM–GN.

CV, LSV with a rotating disk electrode (RDE) and chronoamperometry are all used to determine the electroactivities of the catalyst. The Ag loading mass values are 1.59 $\times 10^{-2}$ mg and 1.32 $\times 10^{-2}$ mg for Ag NN@POM and Ag NN@POM–GN respectively. From Figs. 16(a) and 16(b) we can see that the two hybrids have electrocatalytic activities for ORR. Compared with the Ag NN@POM, the Ag NN@POM–GN has cathode peaks that show a significant positive shift and a higher current density, indicating enhanced electrocatalytic activity. Figure 16(c) discloses the effect of methanol on the electroactivity of the hybrid. It is surprising to see that the two ORR potentials and the current density have no change after the addition of methanol.

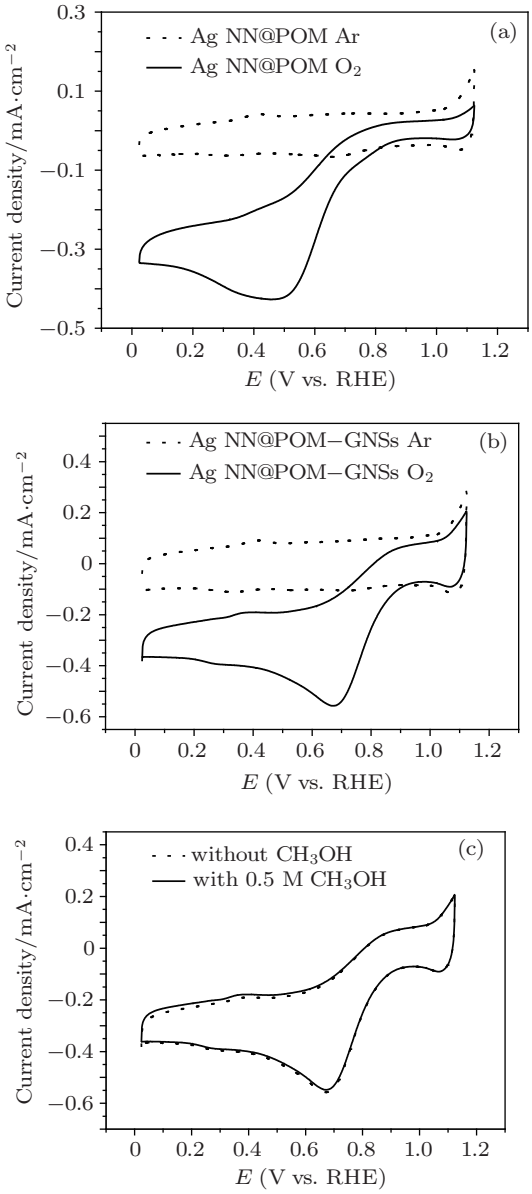


Fig. 16. Cyclic voltammetry curves of ORR on Ag NN@POM (a) and Ag NN@POM–GN (b) in Ar (dotted line)- and O_2 (solid line)-saturated 0.1-M NaOH solutions at a scan rate of 50 $mV \cdot s^{-1}$. Cyclic voltammetry curves for the influence of methanol over Ag NN@POM–GN in O_2 saturated 0.1-M NaOH/0.5-M methanol solutions at a scan rate of 50 $mV \cdot s^{-1}$ (c). Reproduced with permission from Ref. [22].

Figures 17(b) and 17(d) show the Koutecky–Levich plots at several potentials from LSV curves of the two RDE modified electrodes. The slopes of the Koutecky–Levich plots indicate that the ORR catalysis by Ag NN@POM and Ag NN@POM–GN takes a four-electron pathway with high efficiency. The LSV Patterns of the as-prepared Ag-based hybrids and Pt–C with the same loading are integrated together in Fig. 18(a). We can see that the onset potential of the hybrid is largely positive than that of Pt–C.

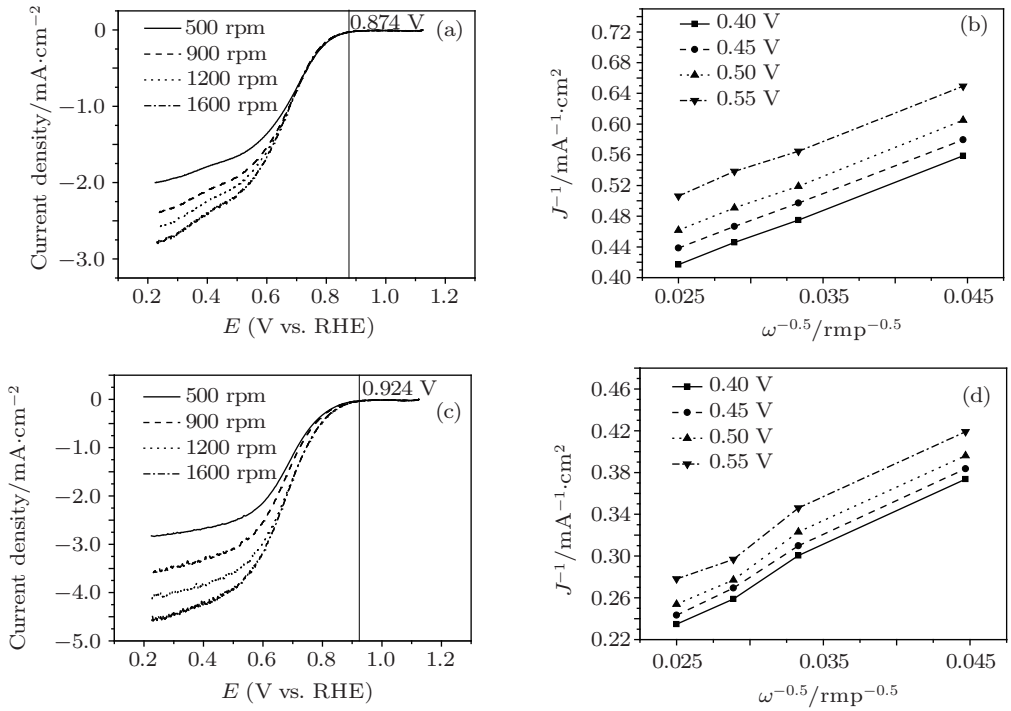


Fig. 17. LSV curves of ORR at various rotation rates for Ag NN@POM (a) and Ag NN@POM–GN (c) in O_2-saturated 0.1-M NaOH solutions at a scan rate of 10 mV · s^{-1}. (b), (d) The Koutecky–Levich plots for panels (a) and (c) at various potentials, respectively. Reproduced with permission from Ref. [22].

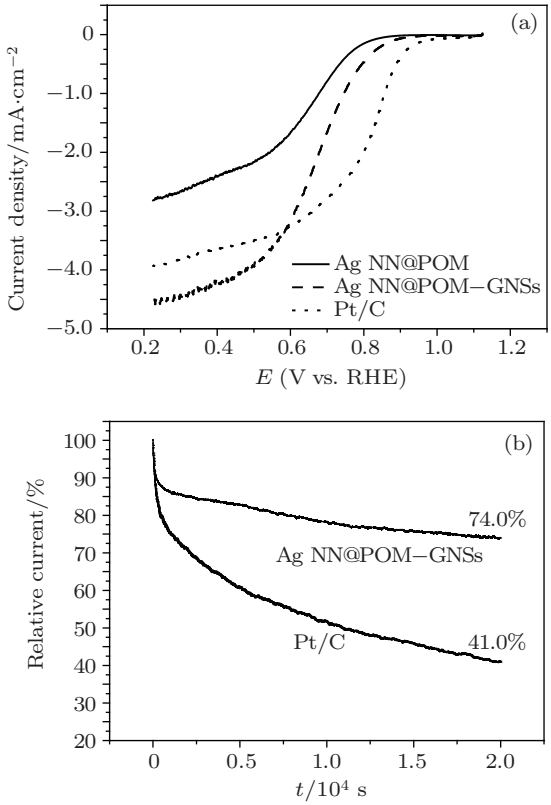


Fig. 18. (color online) (a) Comparison among LSV curves of ORR in O_2-saturated 0.1-M NaOH solutions at a scan rate of 10 mV · s^{-1}. The rotation rate is 1600 rpm. (b) Current–time (i–t) chronoamperometric responses of Ag NN@POM–GN and Pt–C modified GC electrodes at 0.67 V versus RHE in O_2-saturated 0.1 M NaOH at a rotation rate of 1600 rpm. Reproduced with permission from Ref. [22].

The 2×10^4 s stability experiment shows that our catalyst is more stable Than Pt–C (Fig. 18(b)). Thus, the Ag NN@POM–GN may be a new promising low cost ORR electrocatalyst in alkaline media.

3.2.3. Pt NP@POM–GN and Pd NP@POM–GN hybrids with high catalytic activities for methanol and formic acid oxidation

Methanol and formic acid are common fuels used in fuel cells. It is of great importance to develop catalysts toward methanol and formic acid oxidation reaction with high activity. Pt-based and Pd-based materials have been proven to be good catalysts toward the two reactions. Our Pt NPs@POM–GN and Pd NPs@POM–GN are extensions of these works.

Figures 19(a) and 19(c) show a comparison of catalytic activity between two different carbon-based materials. It can be seen that the graphene-based Pt and Pd materials each have a stronger response toward methanol and formic acid oxidation, suggesting a higher catalytic activity. Because durability is a major concern in fuel cells, figures 19(b) and 19(d) demonstrate chronoamperometric curves for the oxidation of methanol (0.60 V versus SCE) and the oxidation of formic acid (0.15 V versus SCE) for Pt and Pd catalysts, respectively. After 1200 s, the residual relative currents for Pt and Pd NPs@POM–GN are about 7.4 and 10.4 times higher than those for Pt and Pd NPs@POM–CB, respectively, indicating the good stability and activity of the Pt and Pd NPs@POM–GN.

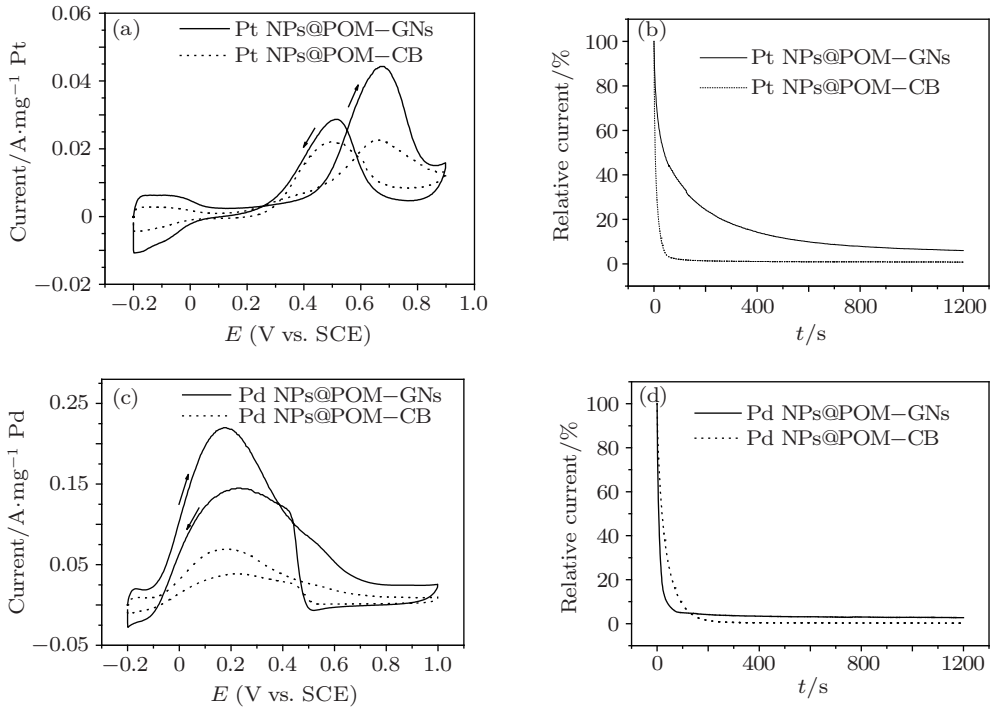


Fig. 19. CV curves of (a) Pt NP@POM–GN and Pt NP@POM–CB catalysts in 0.5-M CH_3OH + 0.5-M H_2SO_4 at a scan rate of 50 $mV \cdot s^{-1}$ and (c) Pd NP@POM–GN and Pd NP@POM–CB catalysts in 0.5-M HCOOH + 0.5-M H_2SO_4 at a scan rate of 50 $mV \cdot s^{-1}$. (b) and (d) Current–time chronoamperometric responses in the above electrolytes at 0.6 V and 0.15 V for Pt and Pd catalysts corresponding to panels (a) and (c), respectively. Reproduced with permission from Ref. [24].

We attribute the better performances of Pt and Pd NPs@POM–GN to the following three major factors: (i) GN with high surface area and 2D flat planes exhibits substantial advantages with regard to mass and charge transport by providing shorter effective lengths for both electronic and ionic transport, a higher electrode/electrolyte contact area, and in some cases also interfacial local effects;[70] (ii) well dispersed metal NPs with small size have beneficial electrocatalytic activities; (iii) the existence of POM in the hybrids may be helpful for the electrocatalytic activities and anti-poisoning properties of the catalysts.

3.3. Brief summary

All the nanohybrids, as photo-electrocatalysts, show fantastic potential applications. To be specific, owing to the high sensitivity and selectivity, good long-term stability, wide linear range, low detection limit, and fast response to H_2O_2 detection, the Au NPs@POM–GN will be potentially used in enzyme-free biosensors for H_2O_2. Salient electrocatalytic activity toward the oxygen reduction reaction and higher durability in alkaline medium of the Ag NN@POM–GN are also revealed, proving the rationality of our surmise that the new hybrid may be a promising cathode material for alkaline fuel cells. The Ag NPs@POM–GNs are new promising low cost cathode materials for alkaline fuel cells. Finally, materials prepared in this way are worth further investigation.

4. Conclusions and perspective

In this review, we introduce a new synthetic strategy of CNTs/GN-based nanomaterials. As discussed above, the resulting novel tri-component hybrids combine properties of their components, thereby enhancing their catalytic activity. These materials can be used in various fields including fuel cells, photosensitizers, and enzyme-free biosensors for H_2O_2. POM plays an important role in photo-electrocatalytic activity of multi-component hybrids. In the long term, finding a desirable POM to help develop co-friendly, reliable catalysts and developing low cost synthetic routes for the production of catalysts is the intention.

References

[1] Yu M F, Lourie O, Dyer M J, Moloni K, Kelly T F and Ruoff R S 2000 *Science* **287** 637
[2] Rao C N R, Sood A K, Subrahmanyam K S and Govindaraj A 2009 *Angewandte Chemie International Edition* **48** 7752
[3] Nanot S, Hároz E H, Kim J H, Hauge R H and Kono J 2012 *Adv. Mater.* **24** 4977
[4] Sun X, Sun H, Li H and Peng H 2013 *Adv. Mater.* **25** 5153
[5] Byrne M T and Gun'ko Y K 2010 *Adv. Mater.* **22** 1672
[6] Jeon I Y, Choi H J, Ju M J, Choi I T, Lim K, Ko J, Kim H K, Kim J C, Lee J J, Shin D, Jung S M, Seo J M, Kim M J, Park N, Dai L and Baek J B 2013 *Sci. Rep.* **3** doi: 10.1038/srep02260
[7] Liang Y, Li Y, Wang H, Zhou J, Wang J, Regier T and Dai H 2011 *Nat. Mater.* **10** 780

[8] Wang S, Yu D and Dai L 2011 *J. Am. Chem. Soc.* **133** 5182
[9] Reiss G and Hütten A 2005 *Nat. Mater.* **4** 725
[10] Singamaneni S, Bliznyuk V N, Binek C and Tsymbal E Y 2011 *J. Mater. Chem.* **21** 16819
[11] Georgakilas V, Gournis D, Tzitzios V, Pasquato L, Guldi D M and Prato M 2007 *J. Mater. Chem.* **17** 2679
[12] Sau T K, Rogach A L, Jäckel F, Klar T A and Feldmann J 2010 *Adv. Mater.* **22** 1805
[13] Kong L, Lu X and Zhang W 2008 *J. Solid State Chem.* **181** 628
[14] Zhu M and Diao G 2011 *Nanoscale* **3** 2748
[15] Quinn B M, Dekker C and Lemay S G 2005 *J. Am. Chem. Soc.* **127** 6146
[16] Li W, Liang C, Zhou W, Qiu J, Zhou Z, Sun G and Xin Q 2003 *J. Phys. Chem. B* **107** 6292
[17] Kongkanand A, Vinodgopal K, Kuwabata S and Kamat P V 2006 *J. Phys. Chem. B* **110** 16185
[18] Li S, Yu X, Zhang G, Ma Y, Yao J, Keita B, Louis N and Zhao H 2011 *J. Mater. Chem.* **21** 2282
[19] Li S, Yu X, Zhang G, Ma Y, Yao J and De Oliveira P 2011 *Carbon* **49** 1906
[20] Liu R, Li S, Yu X, Zhang G, Ma Y and Yao J 2011 *J. Mater. Chem.* **21** 14917
[21] Liu R, Li S, Yu X, Zhang G, Zhang S, Yao J, Keita B, Nadjo L and Zhi L 2012 *Small* **8** 1398
[22] Liu R, Yu X, Zhang G, Zhang S, Cao H, Dolbecq A, Mialane P, Keita B and Zhi L 2013 *J. Mater. Chem. A* **1** 11961
[23] Liu R, Li S, Zhang G, Dolbecq A, Mialane P and Keita B 2014 *J. Cluster Sci.* **25** 711
[24] Liu R, Li S, Yu X, Zhang G, Zhang S, Yao J and Zhi L 2012 *J. Mater. Chem.* **22** 3319
[25] Pradeep C P, Long D L and Cronin L 2010 *Dalton Transactions* **39** 9443
[26] Guo Y and Hu C 2007 *J. Mol. Catalysis A: Chemical* **262** 136
[27] Dolbecq A, Mialane P, Secheresse F, Keita B and Nadjo L 2012 *Chem. Commun.* **48** 8299
[28] Keita B and Nadjo L 2007 *J. Mol. Catalysis A: Chemical* **262** 190
[29] Kirubaharan C J, Kalpana D, Lee Y S, Kim A, Yoo D J, Nahm K S and Kumar G G 2012 *Ind. & Eng. Chem. Res.* **51** 7441
[30] Gao J, Liang G, Cheung J S, Pan Y, Kuang Y, Zhao F, Zhang B, Zhang X, Wu E X and Xu B 2008 *J. Am. Chem. Soc.* **130** 11828
[31] Xu Z, Hou Y and Sun S 2007 *J. Am. Chem. Soc.* **129** 8698
[32] Graeser M, Pippel E, Greiner A and Wendorff J H 2007 *Macromolecules* **40** 6032
[33] Krämer J, Redel E, Thomann R and Janiak C 2008 *Organometallics* **27** 1976
[34] Gonzalez C M, Liu Y and Scaiano J 2009 *J. Phys. Chem. C* **113** 11861
[35] Hong G H and Kang S W 2012 *Ind. & Eng. Chem. Res.* **52** 794
[36] Liu T, Zhang Y, Shao H and Li X 2003 *Langmuir* **19** 7569
[37] Zhang G, Keita B, Dolbecq A, Mialane P, Sécheresse F, Miserque F and Nadjo L 2007 *Chem. Mater.* **19** 5821
[38] Keita B, Zhang G, Dolbecq A, Mialane P, Sécheresse F, Miserque F and Nadjo L 2007 *J. Phys. Chem. C* **111** 8145
[39] Zhang G, Keita B, Biboum R N, Miserque F, Berthet P, Dolbecq A, Mialane P, Catala L and Nadjo L 2009 *J. Mater. Chem.* **19** 8639
[40] Biboum R N, Keita B, Franger S, Nanseu Njiki C P, Zhang G, Zhang J, Liu T, Mbomekalle I M and Nadjo L 2010 *Materials* **3** 741
[41] Keita B, Liu T and Nadjo L 2009 *J. Mater. Chem.* **19** 19
[42] Marcì G, García-López E I and Palmisano L 2014 *Eur. J. Inorg. Chem.* **2014** 21
[43] Xing X, Liu R, Yu X, Zhang G, Cao H, Yao J, Ren B, Jiang Z and Zhao H 2013 *J. Mater. Chem. A* **1** 1488
[44] Gewirth A A and Thorum M S 2010 *Inorg. Chem.* **49** 3557
[45] Yang Y and Zhou Y 1995 *J. Electroanalyt. Chem.* **397** 271
[46] Blizanac B, Ross P and Markovic N 2007 *Electrochimica Acta* **52** 2264
[47] Lee C L, Chiou H P, Syu C M and Wu C C 2010 *Electrochem. Commun.* **12** 1609
[48] Lee C L, Chiou H P, Syu C M, Liu C R, Yang C C and Syu C C 2011 *Int. J. Hydrogen Energy* **36** 12706
[49] Wang S, Yu D, Dai L, Chang D W and Baek J B 2011 *ACS Nano* **5** 6202
[50] Zheng F, Mu G, Zhang Z, Shen Y, Zhao M and Pang G 2012 *Mater. Lett.* **68** 453
[51] Yang Z, Zhou X, Nie H, Yao Z and Huang S 2011 *ACS Appl. Mater. & Interfaces* **3** 2601
[52] Choi H C, Shim M, Bangsaruntip S and Dai H 2002 *J. Am. Chem. Soc.* **124** 9058
[53] Qu L and Dai L 2005 *J. Am. Chem. Soc.* **127** 10806
[54] Chen W, Fan Z, Pan X and Bao X 2008 *J. Am. Chem. Soc.* **130** 9414
[55] Wasmus S and Küver A 1999 *J. Electroanal. Chem.* **461** 14
[56] Wu W and Lin Y T 2010 *Ind. & Eng. Chem. Res.* **49** 5725
[57] Lin Y, Cui X, Yen C H and Wai C M 2005 *Langmuir* **21** 11474
[58] Lin Y, Cui X, Yen C and Wai C M 2005 *J. Phys. Chem. B* **109** 14410
[59] Guo S, Dong S and Wang E 2010 *Adv. Mater.* **22** 1269
[60] Zheng S F, Hu J S, Zhong L S, Wan L J and Song W G 2007 *J. Phys. Chem. C* **111** 11174
[61] Huang C, Li C and Shi G 2012 *Energy & Environ. Sci.* **5** 8848
[62] Chang H and Wu H 2012 *Adv. Func. Mater.* **23** 1984
[63] James D K and Tour J M 2012 *Accounts Chem. Res.* **46** 2307
[64] Kostowskyj M, Kirk D and Thorpe S 2010 *Int. J. Hydrogen Energy* **35** 5666
[65] Kostowskyj M, Gilliam R, Kirk D and Thorpe S 2008 *Int. J. Hydrogen Energy* **33** 5773
[66] Zhou Y, Ma R, Ebina Y, Takada K and Sasaki T 2006 *Chem. Mater.* **18** 1235
[67] Chen W, Cai S, Ren Q Q, Wen W and Zhao Y D 2012 *Analyst.* **137** 49
[68] Pang H, Gao F, Chen Q, Liu R and Lu Q 2012 *Dalton Transactions* **41** 5862
[69] Li W, Kuai L, Qin Q and Geng B 2013 *J. Mater. Chem. A* **1** 7111
[70] Nohra B, El Moll H, Rodriguez Albelo L M, Mialane P, Marrot J, Mellot-Draznieks C, O'Keeffe M, Ngo Biboum R, Lemaire J and Keita B 2011 *J. Am. Chem. Soc.* **133** 13363